Mon. Not. R. Astron. Soc. **306,** 137–152 (1999)

The shape of the blue/UV continuum of B3-VLA radio quasars: dependence on redshift, blue/UV luminosity and radio power

Ruth Carballo,[1,2]★ J. Ignacio González-Serrano,[1] Chris R. Benn,[3] Sebastian F. Sánchez[1,2] and Mario Vigotti[4]

[1]*Instituto de Física de Cantabria (CSIC-Universidad de Cantabria), Facultad de Ciencias, 39005 Santander, Spain*
[2]*Departamento de Física Moderna, Universidad de Cantabria, Facultad de Ciencias, 39005 Santander, Spain*
[3]*Isaac Newton Group of Telescopes, Royal Greenwich Observatory, Apdo. de correos 321, 38780 Santa Cruz de La Palma, Tenerife, Spain*
[4]*Istituto di Radioastronomia, CNR, via Gobetti 101, 40129 Bologna, Italy*

Accepted 1999 January 20. Received 1999 January 20; in original form 1998 August 20

ABSTRACT

We present *UBVR* photometry of a sample of 73 radio quasars, about 80 per cent complete, with redshifts 0.4–2.8. From these data the shape of the spectral energy distribution (SED) in the rest-frame blue/ultraviolet is analysed, using the individual sources as well as through broad-band composite SEDs. The SEDs of the individual sources are generally well fitted with power laws, with slopes α ranging from 0.4 to –1.7 ($S_\nu \propto \nu^\alpha$). Two sources with $\alpha < -1.6$ were excluded from the general study for having very red SEDs, significantly deviating with respect to the remaining sources. The composite SEDs cover the range $\simeq$1300–4500 Å and the only emission feature apparent from the broad-band spectra is the C IV λ1549 line, in agreement with expectations from line equivalent width measurements of radio-loud quasars from the literature. The shape of the composites in the $\log S_\nu$–$\log \nu$ plane exhibits a break at around 3000 Å where the spectrum changes from $\alpha_{\rm blue} = 0.11 \pm 0.16$ at $\lambda > 3000$ Å to $\alpha_{\rm UV} = -0.66 \pm 0.15$ at $\lambda < 3000$ Å. Although the broad-band spectral points are expected to include some masked contamination from emission lines/bumps, the break cannot be explained by line/bump emission, and most likely reflects an intrinsic trend in the continuum.

The continuum shape is shown to depend on redshift. For the quasars with $z < 1.2$ we find $\alpha_{\rm blue} = 0.21 \pm 0.16$ and $\alpha_{\rm UV} = -0.87 \pm 0.20$, i.e. a higher steepening. For $z > 1.2$, $\alpha_{\rm UV}$ is more flat, -0.48 ± 0.12, and there are too few spectral points longward of 3000 Å to obtain $\alpha_{\rm blue}$ and analyse the presence of the 3000-Å break. A trend similar to that between $\alpha_{\rm UV}$ and z is found between $\alpha_{\rm UV}$ and luminosity at 2400 Å, L_{2400}, with luminous quasars exhibiting a harder spectrum.

The data show an intrinsic correlation between L_{2400} and the radio power at 408 MHz, not related to selection effects or independent cosmic evolution. The correlations $\alpha_{\rm UV}$–z, $\alpha_{\rm UV}$–L_{2400} and L_{2400}–z appear to be consistent with accretion disc models with approximately constant black hole mass and accretion rates decreasing with time. If the trends L_{2400}–z and P_{408}–z are predominantly related to a selection bias, rather than cosmic evolution, only one of the correlations $\alpha_{\rm UV}$–L_{2400} or $\alpha_{\rm UV}$–z needs to be intrinsic.

Key words: galaxies: active – galaxies: photometry – quasars: general – ultraviolet: galaxies.

1 INTRODUCTION

The study of the shape of the optical/ultraviolet (UV) continuum of quasars is an essential tool to test the different emission models invoked to explain the observed radiation, and understand their characteristic parameters. Whereas the overall quasar spectrum from the infrared to the X-ray has approximately a power-law form, $S_\nu \propto \nu^\alpha$, with spectral index about -1, in the optical/UV region there is a bump on top of the power-law continuum known as the big blue bump (Elvis et al. 1994; Sanders et al. 1989). The big blue bump is generally interpreted with a two-component model, consisting of the underlying power-law and blackbody-like emission from an accretion disc (AD) around a massive black hole (Malkan 1983; Czerny & Elvis 1987). The determination of the

★E-mail: carballo@ifca.unican.es

shape and strength of the ionizing UV continuum is essential to constrain the accretion disc parameters, for the modelling of the broad-line region of quasars, and other aspects such as the determination of the *k*-corrections for quasars, which affect the derivation of their luminosity functions.

Empirically, the shape of the optical/UV continuum of quasars is generally parametrized by a power law, although this is a local approximation, with the overall shape being more complicated. Measurements of the optical/UV continuum shape at fixed rest-frame wavelengths have been obtained by O'Brien, Gondhalekar & Wilson (1988), and more recently by Natali et al. (1998), on the basis of low-resolution spectroscopic data. O'Brien et al. selected their quasars from availability of *IUE* spectra and published X-ray fluxes, and found a mean spectral index of -0.67 ± 0.05 for the range 1900–1215 Å. The spectral index distribution of radio-loud and radio-quiet quasars appeared to be similar. The authors found a small hardening with redshift, with α ranging from -0.87 ± 0.07 for $z < 1.1$ to -0.46 ± 0.05 for $z > 1.1$, and a trend with luminosity at 1450 Å, in the sense that the more luminous quasars had harder spectra. From a joint regression analysis including spectral index, redshift and luminosity, the authors concluded that the dominant correlation was between α and z, and that the trend between α and luminosity was the result of the correlation of both variables with redshift. Natali et al. (1998) used a complete sample of optically selected radio-quiet quasars, and found that the spectra in the range 5500–1200 Å showed an abrupt change around the so-called '3000-Å emission feature' (Wills, Netzer & Wills 1985), with $\alpha \simeq 0.15$ for $\lambda > 3000$ Å and $\alpha \simeq -0.65$ for $\lambda < 3000$ Å.

Francis et al. (1991) analysed the composite spectrum obtained from optical spectra of around 700 quasars from the Large Bright Quasar Survey (LBQS) (Hewett et al. 1991). The individual spectra yielded slopes ranging from 1 to –1.5 and a median value $\alpha = -0.3$ in the range 5800–1300 Å. Francis et al. fitted to the composite spectrum a curved underlying continuum (a cubic spline), corresponding to $\alpha \simeq 0.0$ for $\lambda > 3000$ Å and $\alpha \simeq -0.6$ below this limit. The authors noted that the high-luminosity quasars had harder spectra than the low-luminosity ones.

The samples studied by Francis et al. (1991) and Natali et al. (1998) select quasars on the basis of the presence of UV excess (although the LBQS includes additional independent selection criteria), and are then biased against quasars with red colours. A similar bias is likely present in the data of O'Brien et al. (1988), who selected the quasars by availability of UV and X-ray measurements. In this paper we present a study of the shape of the blue/UV spectrum of quasars from the B3-VLA Quasar Sample (Vigotti et al. 1997) selected in radio, at 408 MHz. Optical selection biases are significantly lessened in this sample, allowing for a thorough investigation of the shape of their blue/UV spectrum. Since the B3-VLA quasars have been selected at a low frequency, where steep-spectrum, extended emission dominates, the sample minimizes the inclusion of core-dominated quasars, for which an additional component of relativistically beamed optical synchrotron is likely present (Browne & Wright 1985).

The analysis of the blue/UV continuum of the B3-VLA quasars is based on *UBVR* photometry of around 70 sources, with redshifts in the range 0.4–2.8. The quasar SEDs are studied both individually and from created composite spectra, and the dependence of the blue/UV slope and luminosity on redshift and radio properties is analysed.

Near-infrared *K*-band imaging of 52 quasars in this work was presented by Carballo et al. (1998). For 16 sources the images revealed extended emission, most likely related to starlight emission from the host galaxy.

2 THE SAMPLE

The B3 survey (Ficarra, Grueff & Tomassetti 1985) catalogues sources to a radio flux density limit $S_{408\,\mathrm{MHz}} = 0.1$ Jy. From the B3 Vigotti et al. (1989) selected 1050 radio sources, the B3-VLA Sample, consisting of five complete subsamples in the flux density ranges 0.1–0.2, 0.2–0.4, 0.4–0.8, 0.8–1.6 and $S_{408} > 1.6$ Jy, all mapped at the VLA. Candidate quasar identifications (objects of any colour appearing star-like to the eye) were sought on the POSS-I red plates down to the plate limit, $R \simeq 20$, yielding a sample of 172 quasar candidates. Optical spectroscopy was obtained for all the candidates and 125 were confirmed as quasars, forming the B3-VLA Quasar Sample. The sample covers the redshift range $z = 0.4$–2.8, with mean redshift $z = 1.16$, and radio powers $P_{408\,\mathrm{MHz}} \sim 10^{33}$–$10^{36}$ erg s^{-1} Hz^{-1} (adopting $H_0 = 50$ km s^{-1} Mpc^{-1} and $\Omega_0 = 1$). The sample of quasar candidates and the final B3-VLA Quasar Sample are described in Vigotti et al. (1997). The optical incompleteness of the radio quasar sample, i.e. the fraction of quasars fainter than the optical limit of $R \simeq 20$ mag, depends on the radio flux. From *R*-band photometry of the complete radio quasar sample presented by Willot et al. (1998), we infer that the fraction of radio quasars with $R > 20$ is 35 per cent for the flux range $0.4 < S_{408} < 1.0$ Jy (mean flux density 0.66 Jy) and 45 per cent for 0.2–0.4 Jy (mean flux density 0.28 Jy). The average $B - R$ colour of these quasars is 0.6 (similar to the value we found for the B3-VLA quasars in Section 4.2). For the quasars with $S_{408} > 1$ Jy we can use the distribution of *B*-band magnitudes obtained by Serjeant et al. (1998) for the Molonglo-APM Quasar Survey (average flux density $S_{408} \sim 1.7$ Jy). Adopting as limit $B = 20.6$, equivalent to $R = 20$ for typical radio quasar colours, the fraction of quasars with $S_{408} > 1$ Jy fainter than this limit is around 15 per cent.

The B3-VLA Quasar Sample contains 64 quasars with $S > 0.8$ Jy and average flux density of 2.25 Jy, 32 with $S = 0.4$–0.8 Jy and average flux density of 0.53 Jy, and 29 quasars with $S = 0.1$–0.4 Jy and average flux density of 0.22 Jy. Adopting for the three groups optical incompleteness of 15, 25 and 45 per cent respectively, the estimated optical completeness for the total sample would be around 75 per cent, improving to 80 per cent for $S > 0.4$ Jy.

The present work is based on *UBVR* photometry of a representative group of 73 quasars from the B3-VLA Quasar Sample. The quasars were selected to have right ascensions (RA) in the range 7^{h}–15^{h} and comprise the 44 with $S_{408} > 0.8$ Jy, the 23 with $0.4 < S_{408} < 0.8$ Jy, the four with $0.3 < S_{408} < 0.4$, and two out of 15 with $0.1 < S_{408} < 0.3$. The sample is equivalent to the Quasar Sample (except for the RA constraint) for $S > 0.4$ Jy, and includes only a few quasars with fainter radio fluxes, although generally close to the limit. We estimate therefore the optical completeness of the studied sample to be about 80 per cent.

3 OBSERVATIONS, DATA REDUCTION AND PHOTOMETRIC CALIBRATION

The optical images were obtained on 1997 February 5−8, using a 1024×1024 TEK charge-coupled device (CCD) at the Cassegrain focus of the 1.0-m JKT on La Palma (Spain), and on March 11–12, using a 2048×2048 SITe CCD at the Cassegrain focus of the 2.2-m telescope on Calar Alto (Spain). U, B, V and R standard Johnson filters were used and the pixel scale was 0.33 arcsec pixel^{-1} for the JKT and 0.533 arcsec pixel^{-1} for the 2.2-m telescope. The field of view was $\sim 6 \times 6$ arcmin^2 for all the images. A standard observing procedure was used. Bias and sky flat fields for each night and filter were obtained during the twilight. Faint photometric standards

Table 1. Summary of photometric calibration.

Date	$k(U)$	$k''(U-B)$	rms	$k(B)$	rms	$k(V)$	rms	$k(R)$	rms
5 Feb	1.55 ± 0.15		0.024			0.54 ± 0.12	0.009		
6 Feb	0.34 ± 0.07		0.014			0.12 ± 0.10	0.027		
7 Feb	0.54 ± 0.10		0.051	0.24 ± 0.02	0.012	0.21 ± 0.02	0.020	0.15 ± 0.02	0.015
8 Feb				0.28 ± 0.04	0.021			0.11 ± 0.01	0.008
11 Mar	0.48 ± 0.05	−0.250 ± 0.023	0.042	0.19 ± 0.03	0.028	0.15 ± 0.01	0.013	0.09 ± 0.01	0.008
12 Mar	0.34 ± 0.05	−0.163 ± 0.030	0.052	0.14 ± 0.03	0.042	0.13 ± 0.02	0.027	0.06 ± 0.02	0.022

(Landolt 1992 and references therein) were observed each night in order to obtain the flux calibration. The exposure time was different for each quasar and filter, ranging from 60 to 1200 s, and was set according to the red and blue automated plate measurement (APM) magnitudes from POSS-I. The seeing varied from ∼1.8 arcsec, on February 5, 6, 7 and March 11, to ∼2.2 arcsec on February 8 and March 12. The data were reduced using standard tasks in the IRAF software package [1]. Flat-field correction was better than 0.5 per cent. Large exposure time images were cleaned from cosmic ray hits automatically.

Instrumental magnitudes for the standard stars were measured in circular apertures of 13-arcsec diameter. The flux calibration was obtained, as a first step, assuming no colour effects in any of the bands. For all the nights at both telescopes this assumption was proved to be correct for filters B, V and R. At the U band, for two of the nights, we took colour effects into account, introducing the colour term $-k'(U-B)$. Table 1 lists the results of the photometric calibration showing the extinction and colour coefficients for each night/filter together with the rms of the fits.

All nights were photometric except the second half of February 5, during which we had clouds. In this part of the night we only obtained data for three objects in two bands. The first part of the night was photometric and the calibration data listed in Table 1 correspond to this part of the night.

4 OPTICAL PHOTOMETRY OF THE QUASARS

4.1 *UBVR* magnitudes

Quasar magnitudes were measured on the images using the same apertures as for the photometric standards. In one case (B3 0724+396) a nearby star was included within the aperture and it was subtracted by modelling it with a two-dimensional point spread function (PSF). Measurement errors ranged from less than 0.01 to 0.9 mag, and the typical values were lower than 0.15 mag (85 per cent of the data). Apparent *UBVR* magnitudes, not corrected for Galactic extinction, and their errors are listed in Table 2, along with the observing dates and the colour excess $E(B-V)$ towards each object, obtained from the $N(\mathrm{H\,I})$ maps by Burnstein & Heiles (1982). The redshift and radio power of the sources are also listed in the table.

Some of the quasars (11) were observed with the same filter twice on the same night or on the two runs. In these cases the difference in magnitudes never excedeed 0.2 mag, and the quoted magnitudes correspond to the average value. For three quasars (B3 0836+426, 0859+470 and 0906+430) the U- and V-band data were obtained in the second part of February 5, which was cloudy. We have made a crude estimate of these magnitudes on the basis of the photometric standards measured over the same period, and assigned them an error of ∼ 0.3 mag. These objects, however, have not been used for any further analysis.

For the 70 quasars observed under good photometric conditions rest-frame SEDs were built, using the zero-magnitude flux densities from Johnson (1966; U, B and R bands) and Wamsteker (1981; V band). For the Galactic extinction correction the Rieke & Lebofsky (1985) reddening law was used. The corrections were lower than 0.05 mag for 80 per cent of the sources. For the remaining sources the corrections for the U band, which is the most affected, ranged from 0.05 to 0.56 mag, with a median value of 0.19. Fig. 1 shows the SEDs of the 70 quasars, plotted in order of increasing redshift. The SEDs will always be referred to the $\log S_\nu$–$\log \nu$ plane.

Three sources in Table 2 (B3 0955+387, 1312+393 and 1444+417, see also Fig. 1) have magnitude errors larger than 0.3 mag in several bands. In addition, three sources have abrupt changes in their SEDs (B3 1317+380, 0726+431 and 0922+425), probably related to intrinsic variability or not-understood errors. These six sources will not be considered for the analysis presented in the forthcoming sections.

Histograms of the U, B, V and R magnitudes (corrected for Galactic extinction) for the 64 quasars with good photometry are presented in Fig. 2. The R-band histogram shows that most of the quasars have R magnitudes well below the POSS-I limit of $R \simeq 20$ used for the quasar identifications, confirming that this limit guaranties a rather high optical completeness.

We have indicated in Fig. 1 the wavelengths of the strongest quasar emission lines in the studied range, like Hβ, Mg II λ2798, C III] λ1909, C IV λ1549 and Lyα. For each spectral point on the figure we have plotted the covered full width at half-maximum (FWHM), assuming the standard FWHMs (observer frame) for the U, B, V and R bands from Johnson (1966). We infer from the figure that about 45 per cent of the spectral points do not include within half the filter bandpass the central wavelengths of any of the emission lines listed above. Broader emission features, such as the Fe II and Fe II + Balmer emission bumps in the ranges 2250–2650 and 3100–3800 Å, could also affect the measured broad-band fluxes.

Table 3 presents average equivalent width (EW) measurements of these emission lines for several quasar samples from the literature, which can be used to estimate their average contribution to the broad-band fluxes. The listed EWs include the values obtained by Baker & Hunstead (1995) for Molonglo radio quasars, which is a sample selected at 408 MHz, with $S_{408} > 0.95$ Jy, and therefore appropiate for comparison with our sample (although it does not list the EWs for the Fe II bumps). Also listed are the EW measurements for radio-loud quasars given by Zheng et al. (1997, from a UV composite that extends to 3000 Å) and the EWs for optically selected LBQS quasars from Francis et al. (1991) and Green (1998). Francis et al. (1991) mention that the height of the bumps derived from their work would be decreased if the regions around 1700 and 2650 Å were taken as continuum, although at the cost of a strongly curved continuum. Green (1998) uses as

[1] IRAF is distributed by the NOAO, which is operated by AURA, Inc., under contract to the NSF.

Table 2. Photometry of the B3-VLA quasars.

B3 name	z	$\log P_{408}$ erg s^{-1}Hz^{-1}	U	$\sigma(U)$	B	$\sigma(B)$	V	$\sigma(V)$	R	$\sigma(R)$	Date of obs. $U/B/V/R$	$E(B-V)$
0701+392	1.283	34.99	18.50	0.14	20.11	0.17	19.69	0.12	18.89	0.13	6/8/6/8	0.118
0704+384	0.579	34.72	18.82	0.12	19.08	0.18	18.84	0.14	18.48	0.14	5/7/5/7	0.076
0724+396	2.753	35.18	19.15	0.12	19.93	0.15	18.78	0.04	18.75	0.05	12/12/12/12	0.062
0726+431	1.072	35.00	19.52	0.29	20.25	0.20	18.72	0.13	–	–	6/8/6/-	0.056
0739+397B	1.700	35.11	17.98	0.14	19.01	0.07	18.87	0.14	18.33	0.05	6/11/6/11	0.050
0740+380C	1.063	35.66	17.59	0.17	18.23	0.05	17.65	0.08	17.51	0.04	5/7/5/7	0.043
0756+406	2.016	35.08	19.08	0.20	19.80	0.09	19.24	0.06	18.64	0.06	12/12/12/12	0.048
0802+398	1.800	34.96	19.26	0.12	20.01	0.09	19.97	0.11	19.70	0.15	12/12/12/12	0.030
0821+394	1.216	35.23	17.51	0.18	18.21	0.08	17.39	0.06	17.25	0.04	5/7/5/7	0.034
0821+447	0.893	34.99	17.42	0.16	18.28	0.09	17.64	0.08	17.56	0.06	5/7/5/7	0.039
0827+378	0.914	35.34	17.78	0.05	18.37	0.05	17.94	0.06	17.71	0.03	5/11/5/11	0.028
0829+425	1.056	34.60	18.69	0.20	19.17	0.08	18.93	0.15	18.47	0.05	6/11/6/11	0.030
0836+426	0.595	34.26	20.63	0.30*	20.02	0.17	19.70	0.30*	19.23	0.13	5/7/5/7	0.033
0849+424	0.978	34.84	18.59	0.20	19.72	0.16	18.73	0.19	18.85	0.12	6/8/6/8	0.018
0859+470	1.462	35.28	17.93	0.30*	18.12	0.04	19.49	0.30*	18.07	0.06	5/7/5/7	0.009
0904+386	1.730	34.86	17.73	0.11	18.37	0.06	18.11	0.04	17.77	0.03	12/12/12/12	0.002
0906+430	0.670	35.44	19.18	0.30*	18.96	0.09	20.00	0.30*	18.22	0.07	5/7/5/7	0.009
0907+381	2.16	34.84	16.41	0.07	17.58	0.04	17.47	0.03	17.22	0.03	11/11/12/11	0.010
0910+392	0.638	33.97	18.42	0.08	19.22	0.05	18.81	0.06	18.58	0.05	12/12/12/12	0.002
0913+391	1.250	34.94	18.70	0.19	19.54	0.15	18.80	0.13	18.84	0.12	6/7/6/7	0.000
0918+381	1.108	35.28	20.06	0.49	19.81	0.14	19.23	0.19	18.62	0.08	6/7/6/7	0.002
0922+407	1.876	34.75	19.52	0.14	20.59	0.09	20.42	0.10	19.76	0.11	11/11/11/11	0.002
0922+422	1.750	35.39	18.33	0.12	18.92	0.08	18.36	0.06	17.96	0.05	7/7/7/7	0.006
0922+425	1.879	35.54	19.94	0.29	21.12	0.19	21.01	0.43	18.95	0.07	6/7/6/7	0.006
0923+392	0.698	34.74	15.72	0.09	16.89	0.03	16.62	0.04	16.28	0.02	6/7/6/7	0.005
0926+388	1.630	34.98	19.12	0.18	19.53	0.08	19.42	0.09	19.29	0.09	12/12/12/12	0.000
0935+397	2.493	34.96	21.15	0.34	21.34	0.13	20.89	0.14	20.52	0.21	12/12/12/12	0.005
0937+391	0.618	34.56	17.60	0.16	18.28	0.03	18.23	0.13	18.04	0.05	6/8/6/8	0.003
0945+408	1.252	35.20	17.00	0.14	18.05	0.03	17.70	0.08	17.58	0.04	6/8/6/8	0.000
0951+408	0.783	34.51	18.76	0.11	19.56	0.10	18.77	0.08	18.92	0.05	7/11/7/11	0.001
0953+398	1.179	34.43	18.59	0.08	19.56	0.06	19.14	0.06	18.73	0.04	12/12/12/12	0.000
0955+387	1.405	35.29	20.04	0.33	21.43	0.41	21.66	0.89	21.36	0.34	6/8/6/8	0.004
1007+417	0.613	34.87	15.54	0.07	16.35	0.02	16.05	0.03	16.15	0.02	6/8/6/8	0.000
1015+383	0.380	33.65	16.99	0.06	17.70	0.03	17.59	0.05	17.39	0.05	7/8/7/8	0.000
1020+400	1.250	35.01	16.83	0.11	18.24	0.08	17.83	0.09	17.66	0.06	6/8/6/8	0.000
1030+415	1.120	34.70	18.54	0.11	19.20	0.08	18.85	0.14	18.32	0.05	7/11/7/11	0.000
1105+392	0.781	34.87	19.19	0.34	19.91	0.08	19.17	0.20	18.87	0.07	6/8/6/8	0.000
1109+437	1.680	35.99	18.15	0.14	18.94	0.06	18.85	0.13	18.42	0.05	6/11/6/11	0.000
1111+408	0.734	35.55	16.51	0.08	17.39	0.03	17.26	0.06	–	–	6/8/6/-	0.020
1116+392	0.733	34.01	18.01	0.12	18.62	0.06	18.27	0.04	18.09	0.04	12/12/12/12	0.000
1123+395	1.470	34.63	17.42	0.09	18.47	0.05	18.33	0.04	17.95	0.03	12/12/12/12	0.000
1128+385	1.735	34.44	18.78	0.23	19.13	0.06	18.77	0.06	18.31	0.03	12/12/12/12	0.000
1141+400	0.907	34.28	20.04	0.20	20.25	0.07	19.71	0.08	19.52	0.08	12/12/12/12	0.000
1142+392	2.276	35.33	18.32	0.15	19.04	0.06	18.81	0.06	18.68	0.05	12/12/12/12	0.008
1144+402	1.010	34.43	17.85	0.19	18.82	0.04	18.24	0.08	17.94	0.04	6/8/6/8	0.000
1148+387	1.303	35.27	16.06	0.10	17.33	0.04	17.08	0.05	16.75	0.03	6/8/6/8	0.000
1148+477	0.867	35.05	16.82	0.08	17.53	0.03	17.13	0.03	16.95	0.02	7/11/7/11	0.004
1203+384	0.838	34.42	18.38	0.10	–	–	18.24	0.05	18.14	0.04	7/-/7/11	0.000
1204+399	1.530	34.47	17.26	0.08	18.23	0.05	18.14	0.04	17.83	0.04	12/12/12/12	0.009
1206+439B	1.400	35.79	17.77	0.09	18.45	0.04	17.97	0.04	17.34	0.02	7/11/7/11	0.000
1228+397	2.217	35.26	17.88	0.08	18.54	0.06	18.42	0.06	18.18	0.07	7/7/7/7	0.000
1229+405	0.649	34.31	19.04	0.12	19.39	0.10	19.33	0.14	19.04	0.07	7/11/7/11	0.000
1239+442B	0.610	34.37	17.94	0.07	18.63	0.03	18.39	0.04	18.14	0.03	7,11/11/7,11/11	0.000
1240+381	1.316	34.29	17.86	0.06	19.28	0.05	18.87	0.06	18.43	0.05	12/12/12/12	0.000
1242+410	0.811	34.68	19.71	0.20	–	–	20.02	0.15	19.65	0.13	6/-/6/8	0.000
1247+450A	0.799	34.71	17.05	0.07	17.93	0.03	17.62	0.05	17.47	0.02	7/11/7/11	0.004
1256+392	0.978	34.66	19.22	0.05	19.62	0.10	19.12	0.13	18.85	0.05	7/11/7/11	0.000
1258+404	1.656	35.93	18.32	0.09	18.63	0.05	18.45	0.06	18.18	0.04	7/11/7/11	0.000
1312+393	1.570	35.04	21.41	0.75	22.22	0.30	21.97	0.59	21.76	0.49	11/11/6/11	0.000
1315+396	1.560	35.06	17.75	0.15	18.69	0.04	18.61	0.05	18.20	0.04	11/11/11/11	0.000
1317+380	0.835	34.44	19.65	0.22	20.42	0.17	18.98	0.10	19.64	0.09	7/11/7/11	0.000
1339+472	0.502	34.47	20.13	0.49	20.26	0.11	19.23	0.06	18.74	0.05	6/11/6,12/11	0.006
1341+392	0.768	34.61	20.68	0.29	21.18	0.09	20.80	0.14	20.23	0.14	11/11/7,11,12/11	0.000
1342+389A	1.533	35.15	17.84	0.11	18.41	0.04	18.32	0.04	17.97	0.03	11/11/11/11	0.000

Table 2 – *continued*

B3 name	z	log P_{408} erg s^{-1}Hz^{-1}	U	$\sigma(U)$	B	$\sigma(B)$	V	$\sigma(V)$	R	$\sigma(R)$	Date of obs. $U/B/V/R$	$E(B-V)$
1343+386	1.844	35.31	17.55	0.10	18.10	0.04	17.87	0.03	17.50	0.03	11/11/11/11	0.000
1348+392	1.580	34.88	19.19	0.14	19.99	0.09	19.79	0.08	19.61	0.09	12/12/12/12	0.000
1355+380	1.561	34.93	18.65	0.07	19.48	0.04	19.41	0.07	18.78	0.05	11/11/11/11	0.000
1357+394B	0.804	34.20	18.08	0.06	18.85	0.05	18.53	0.05	18.31	0.04	12/12/12/12	0.000
1416+400	0.473	33.88	19.89	0.15	20.37	0.05	19.94	0.11	19.40	0.09	11/11/11/11	0.000
1417+385	1.832	34.41	18.54	0.07	19.19	0.06	19.03	0.05	18.65	0.06	12/12/12/12	0.000
1419+399	0.622	33.35	18.67	0.12	19.00	0.06	19.01	0.07	18.75	0.03	12/12/12/12	0.000
1435+383	1.600	34.89	17.47	0.09	18.20	0.05	18.04	0.04	17.78	0.04	12/12/12/12	0.000
1444+417A	0.675	34.60	18.73	0.39	19.42	0.21	19.39	0.34	19.08	0.12	6/11/6/11	0.002

*Indicates unreliable photometry (second part of the night of February 5).

continuum the regions 2645–2700, 3020–3100 Å and other wavelengths around 4430 and 4750 Å, and finds that the Fe II + Balmer bump in the range 3100–3800 Å is absent in his composite. The EW for Fe II λ2400 from Green (1998) is very similar to that measured by Zheng et al. (1997).

Baker & Hunstead (1995) obtain qualitative estimates of the contribution of Fe II bumps for different radio morphologies from the height of the composite spectra relative to a power-law continuum from ∼2000 to ∼5000 Å. The authors conclude that the Fe II bumps are absent in lobe-dominated and compact-steep-spectrum quasars, but rather strong in core-dominated quasars, which resemble in various line properties optically selected quasars. The continuum of optically selected quasars is known to curve at around 3000 Å (Francis et al. 1991; Natali et al. 1998), and the strength of the bumps obtained by Baker & Hunstead (1995) will be significantly decreased if the underlying continuum was allowed to curve. Boroson & Green (1992) had previously found that flat-spectrum quasars have stronger Fe II λλ4434–4684 than steep-spectrum ones, and that, as a whole, radio-loud quasars have fainter emission than radio-quiet ones. The latter result was also reported by Cristiani & Vio (1990); Fe II λ2400 is the only Fe II bump revealed in their composite spectra for radio-loud quasars, and the feature, almost absent, is less pronounced than in the composite for radio-quiet quasars. Zheng et al. (1997) derive however a lower EW for Fe II λ2400 for radio-quiet quasars (22 versus 38 Å), showing evidence of the uncertainties in the contribution of these bumps.

Adopting as EWs for the C IV, C III] and Mg II lines the values from the Molonglo sample we infer the maximum contribution to the broad-band fluxes for the C IV line, amounting on average to 25 per cent if the line is included in the U, B or V band. For the C III] line the average contribution is below 7 per cent and for Mg II in the range 6–11 per cent. As EW for Fe II ∼2400 Å we adopted the value for the radio quasar sample by Zheng et al. (1997). The EWs for C IV, C III] and Mg II by Zheng et al. (1997) are in fact very similar to those from the Molonglo quasars, and the radio sample is also very similar to ours in terms of optical luminosity. From the average EW of 38 Å the inferred contribution to the broad-band fluxes is 5–9 per cent. The Fe II + Balmer ∼ 3400 Å feature lies outside the spectral region covered by the composite by Zheng et al., and is absent in the composites by Green (1998) and Cristiani & Vio (1990). Adopting half the EW from Francis et al. (1991), i.e. around 38 Å, its expected contribution would be below 6 per cent when included in the V or R bands.

Table 3. Average equivalent widths of quasar emission lines.

Line	Baker & Hunstead	Zheng et al.	Green	Francis et al.	Adopted
C IV	93	77	68	37	93
C III]	23	17		20	23
Mg II	58	50	53	50	58
Fe II λ2400		38	39	35	38
Fe II λ3400*			absent	76	38
Fe II λ4500			29	41	

*Includes Balmer emission.

4.2 Optical broad-band colours of the quasars

The distribution of the $U-R$, $B-R$ and $U-V$ colours as a function of redshift is shown in Fig. 3. The broad-band colours do not show a clear variation with redshift. If anything, this would be a blueing of the $U-V$ colour with redshift up to z around 2.5. The mean colours derived for these quasars (indicated in the figure with dotted lines) are $\langle U-R\rangle = -0.08$, $\langle B-R\rangle = 0.64$ and $\langle U-V\rangle = -0.38$ with dispersions 0.45, 0.27 and 0.42, respectively, and correspond to observed spectral indices $\alpha_{\mathrm{obs}\,U-R} = -0.50$, $\alpha_{\mathrm{obs}\,B-R} = -0.39$ and $\alpha_{\mathrm{obs}\,U-V} = -0.75$ with dispersions 0.64, 0.53 and 0.96. From the comparison of the $B-R$ and $U-V$ spectral indices a trend is found in the sense that the SED is steeper at higher frequencies, in agreement with the results found by Natali et al. (1998).

5 SPECTRAL ENERGY DISTRIBUTION OF THE INDIVIDUAL SOURCES

In this section we discuss the shape of the individual SEDs of the B3 quasars. The SEDs of the 61 sources with available photometry at the four bands were fitted through χ^2 minimization, using a power-law model (p) and a quadratic model (q). The second model was chosen as a simple representation for the SEDs curved on the $\log S_\nu$–$\log \nu$ plane. A fit was accepted if the probability Q that the χ^2 should exceed the particular measured value by chance was higher than 1 per cent. The best-fit spectral indices and their errors are listed in Table 4. Forty-one quasars have acceptable fits as power laws. Thirty-nine of these have also acceptable fits as quadratics and in six cases the quadratic model gives a significant improvement of the fits (higher than 85 per cent using an F-test). These six cases are labelled as p⟶q in the last column of Table 4. There are cases where the shape of the SED is clearly curved, but a power-law model is acceptable because of the large errors. Similarly, SEDs that resemble power laws to the eye and have small photometric errors may not have acceptable fits for this model. The two sources with acceptable fits as power laws but not as quadratics are B3 0849+424 and 1144+402, and both sources have poor power-law fits ($Q < 0.02$). The SEDs of these sources could be contaminated by emission lines at the U and V bands.

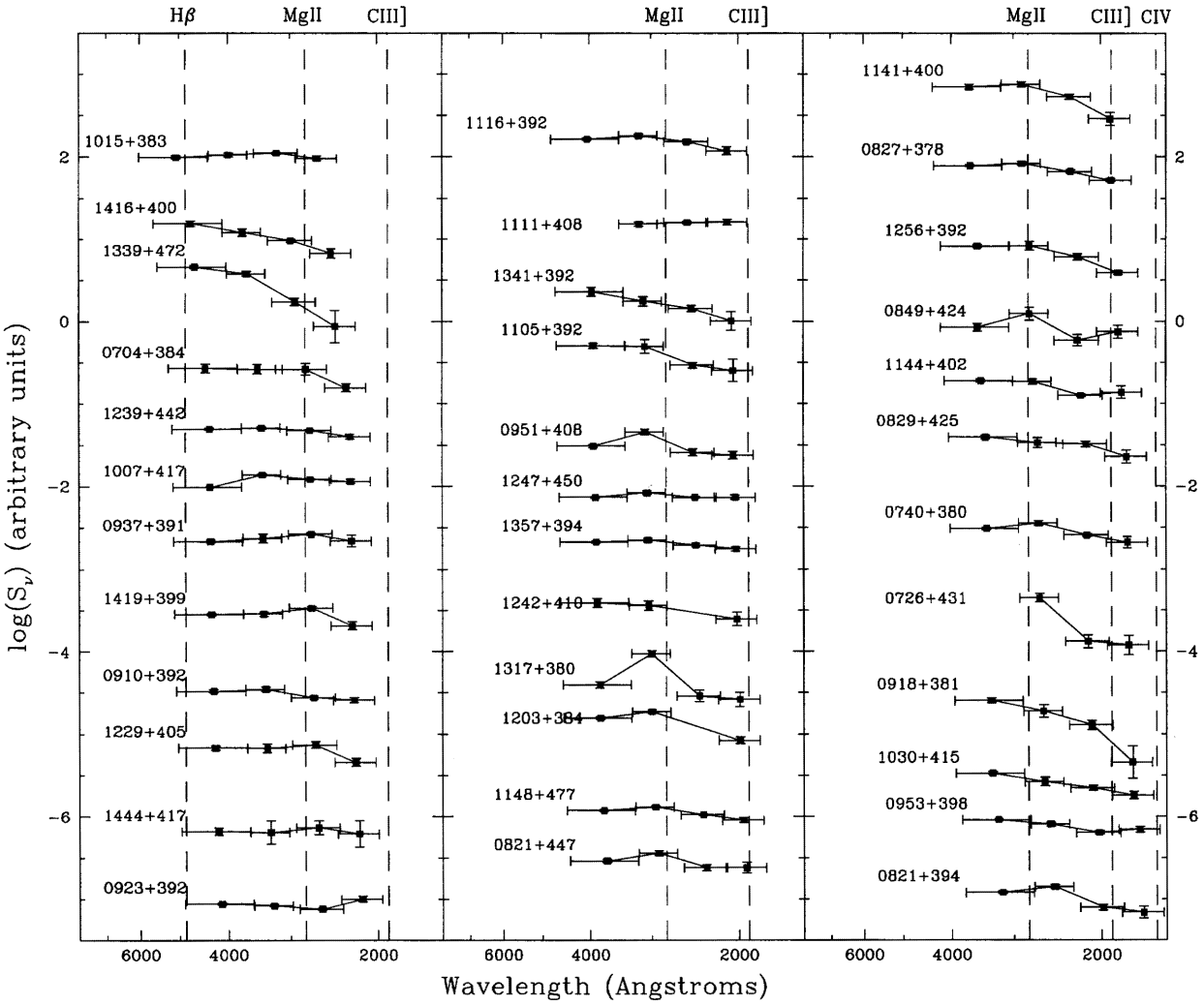

Figure 1. Individual rest-frame SEDs of the B3-VLA quasars plotted in order of increasing redshift. Vertical dashed lines indicate typical broad emission lines observed in quasars: Hβ, Mg II λ2798, C III] λ1909, C IV λ1549 and Lyα.

Table 4. Results of power-law (p) and quadratic (q) fits.

B3 name	α	$\sigma(\alpha)$	Model	B3 name	α	$\sigma(\alpha)$	Model	B3 name	α	$\sigma(\alpha)$	Model
0701+392	0.22	0.25	q	0935+397	-1.10	0.41	p	1228+397	-0.10	0.13	p
0704+384	-0.81	0.25	p	0937+391	0.37	0.11	p	1229+405	-0.32	0.17	q
0724+396	-0.49	0.16	-	0945+408	-0.04	0.08	p	1239+442B	-0.17	0.08	p→q
0739+397B	-0.18	0.14	p→q	0951+408	-0.27	0.14	-	1240+381	-0.09	0.10	-
0740+380C	-0.41	0.12	q	0953+398	-0.56	0.10	p	1247+450A	-0.008	0.07	p
0756+406	-1.18	0.18	p	1007+417	0.44	0.05	-	1256+392	-1.11	0.10	q
0802+398	0.19	0.25	p	1015+383	0.11	0.09	p	1258+404	-0.29	0.10	q
0821+394	-0.68	0.15	-	1020+400	0.20	0.15	-	1315+396	-0.09	0.11	p
0821+447	-0.28	0.16	-	1030+415	-0.90	0.13	p	1339+472	-1.73	0.20	q
0827+378	-0.52	0.07	q	1105+392	-1.16	0.20	p	1341+392	-1.06	0.29	p
0829+425	-0.53	0.17	p	1109+437	-0.18	0.14	p	1342+389A	-0.13	0.09	p
0849+424	-0.41	0.29	p	1116+392	-0.22	0.11	q	1343+386	-0.43	0.08	p
0904+386	-0.37	0.11	p	1123+395	-0.07	0.09	p→q	1348+392	0.02	0.19	p
0907+381	0.36	0.08	p	1128+385	-0.80	0.12	p	1355+380	-0.41	0.11	p
0910+392	-0.40	0.11	p	1141+400	-0.83	0.19	q	1357+394B	-0.27	0.10	p
0913+391	-0.52	0.28	p	1142+392	0.12	0.14	p→q	1416+400	-1.14	0.19	p
0918+381	-1.61	0.28	p	1144+402	-0.85	0.11	p	1417+385	-0.36	0.12	p
0922+407	-0.38	0.22	p→q	1148+387	-0.14	0.08	-	1419+399	0.08	0.11	-
0922+422	-1.02	0.14	p	1148+477	-0.25	0.06	q	1435+383	-0.05	0.01	p
0923+392	-0.22	0.06	-	1204+399	0.15	0.10	p→q				
0926+388	0.12	0.20	p	1206+439B	-1.28	0.08	p				

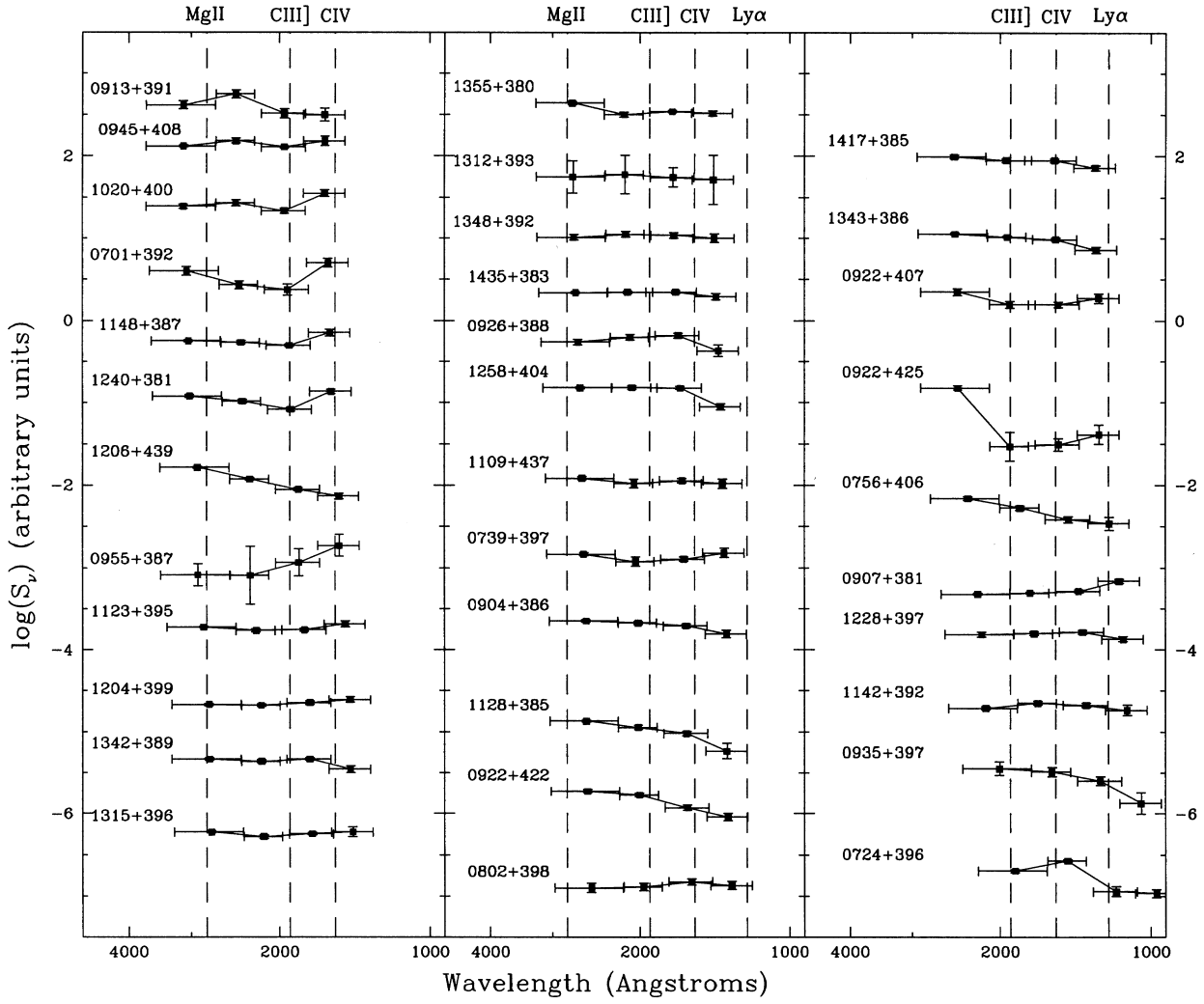

Figure 1. *continued.*

Ten additional quasars without acceptable fits as power laws can be fitted with quadratics. The remaining 10 sources do not have acceptable fits with any of the models (indicated with a hyphen in the last column of Table 4). For some of these sources the lack of good fits could result from the presence of emission peaks in their SEDs related to contamination by emission lines. We note for instance that contamination by C IV could be related to the maxima in the *U* band for B3 1020+400, 1148+387 and 1240+381, and in the *V* band for B3 0724+396.

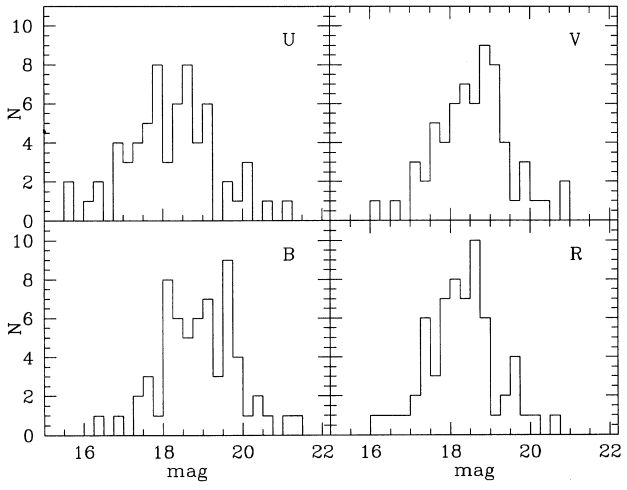

Figure 2. Histograms of the *UBVR* magnitudes for the 64 quasars with good photometry.

Fig. 4 shows the distribution of spectral indices versus redshift for the 61 sources. The slopes were obtained from fixed observed wavelengths, and therefore they correspond to different rest frames (from 2600–5000 for $z = 0.4$ to 1000–1900 for $z = 2.8$). The slopes show a wide range, with values from 0.4 to −1.7, regardless of whether the fits are formally acceptable or not. The mean and the dispersion for the total sample are −0.39 and 0.38 respectively (−0.41 and 0.40 for the sources with formally acceptable power-law fits). The comparison of these values with those obtained from two-band colours (Section 4.2) shows the best agreement for $B - R$, with $\alpha_{\mathrm{obs}\,B-R} = -0.39$ and standard deviation 0.53. The reason for this is that the *B*- and *R*-band errors are low, compared to those for the *U* band, and the errors are weighted for the power-law fits.

Although a mean spectral index was obtained from the sample, the distribution of slopes is asymmetric, showing a tail to steep indices (see Fig. 4 and the histogram in Fig. 5). Considering the total sample of 61 sources, the distribution of spectral indices for $\alpha > -0.9$ is well represented by a Gaussian with a mean of −0.21 and a dispersion of 0.34.

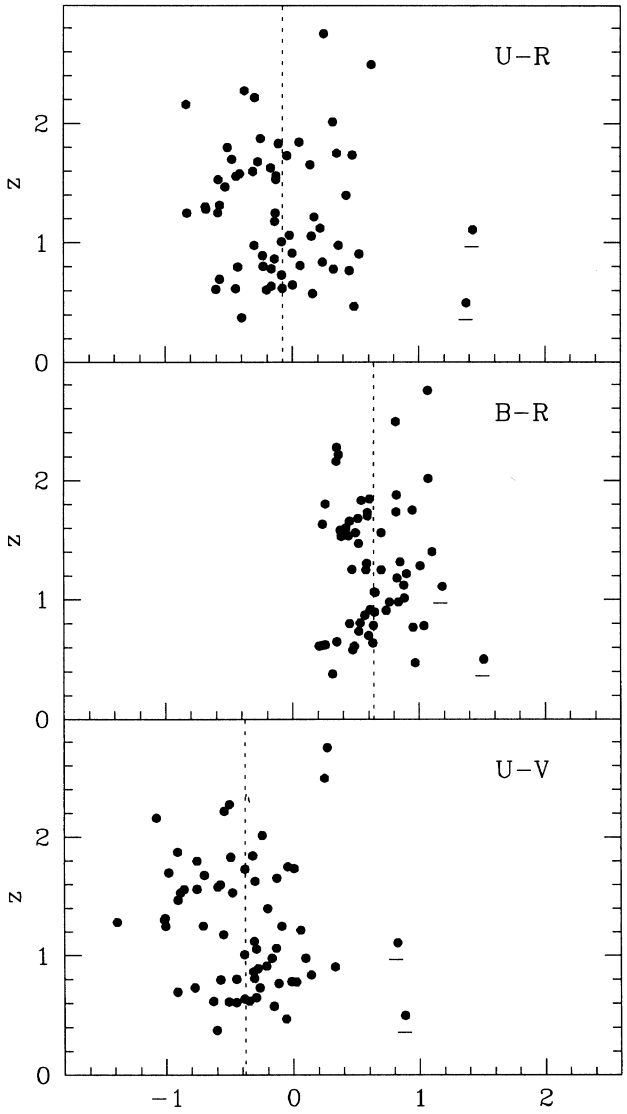

Figure 3. Distribution of the broad-band colours $U-R$, $B-R$ and $U-V$ as a function of redshift. The underlined symbols correspond to the red quasars B3 0918+381 and B3 1339+472 (see Section 6.1).

6 SPECTRAL ENERGY DISTRIBUTION FROM THE COMPOSITE SEDS

6.1 Normalized composite SEDs

The shape of the SED of the quasars can be analysed through a 'composite spectrum', in which the individual SEDs are merged in the rest frame, adopting a specific criterion for the scaling of the fluxes. The coverage of the optical photometry and the range of redshifts of the quasars allows one to study their spectrum in the range ~1300–4500 Å. We chose to normalize the individual SEDs to have the same flux density at a fixed wavelength λ_n *within* the observed range, and the flux density at λ_n was obtained by linear interpolation between the two nearest data points. With this procedure we could not have an appropriate normalization for the whole sample (the coverage for the lowest-redshift quasars is 2500–5000 Å and for the highest-redshift ones 1000–2000 Å); therefore we obtained composite SEDs for different normalization wavelengths. The selected λ_n were 3800, 3500, 3200, 2400, 2200 and 2000 Å and the corresponding normalized SEDs are shown in Fig. 6.

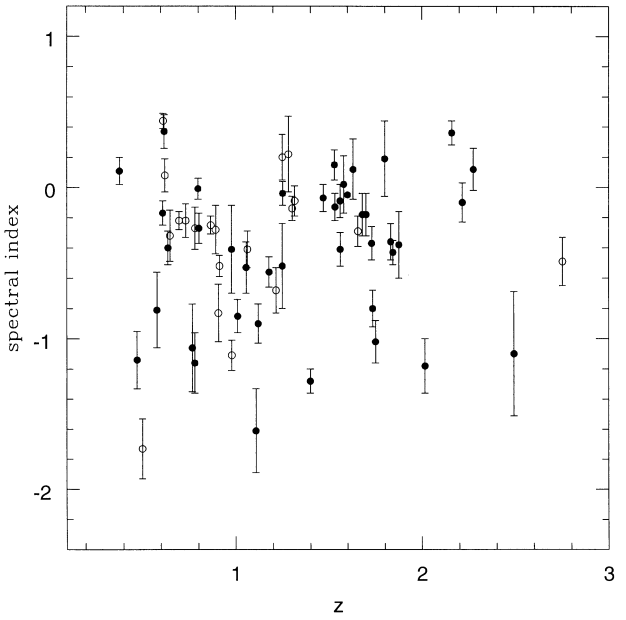

Figure 4. Spectral index versus redshift for the 61 quasars with good photometry and available data in the four bands. Filled circles correspond to power-law fits formally acceptable.

The use of a broad range of values for λ_n is appropriate to analyse the possible dependence of the SED shape with λ_n. The low separation between the λ_n values, typically around 300 Å, allows for a large overlap between the composites and for their comparison in a continuous way. A normalization around 2800 Å was not considered, to avoid the Mg II emission line. The fluxes at the normalization $\lambda_n = 2000$ Å could be contaminated by the weaker C III] λ1909 line, and those at the normalizations 2400, 3200 and 3500 Å by the emission bumps at 2250–2650 and 3100–3800 Å. However, we have seen in Section 4 that the expected contributions of these features are weak; typically below 10 per cent. A 10 per

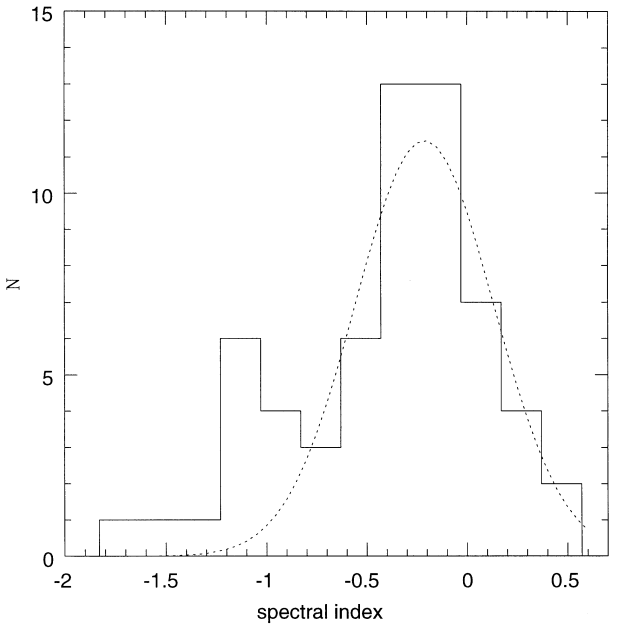

Figure 5. Spectral index distribution for the quasars shown in Fig. 4. The dotted curve shows the Gaussian fit for the quasars with $\alpha > -0.9$.

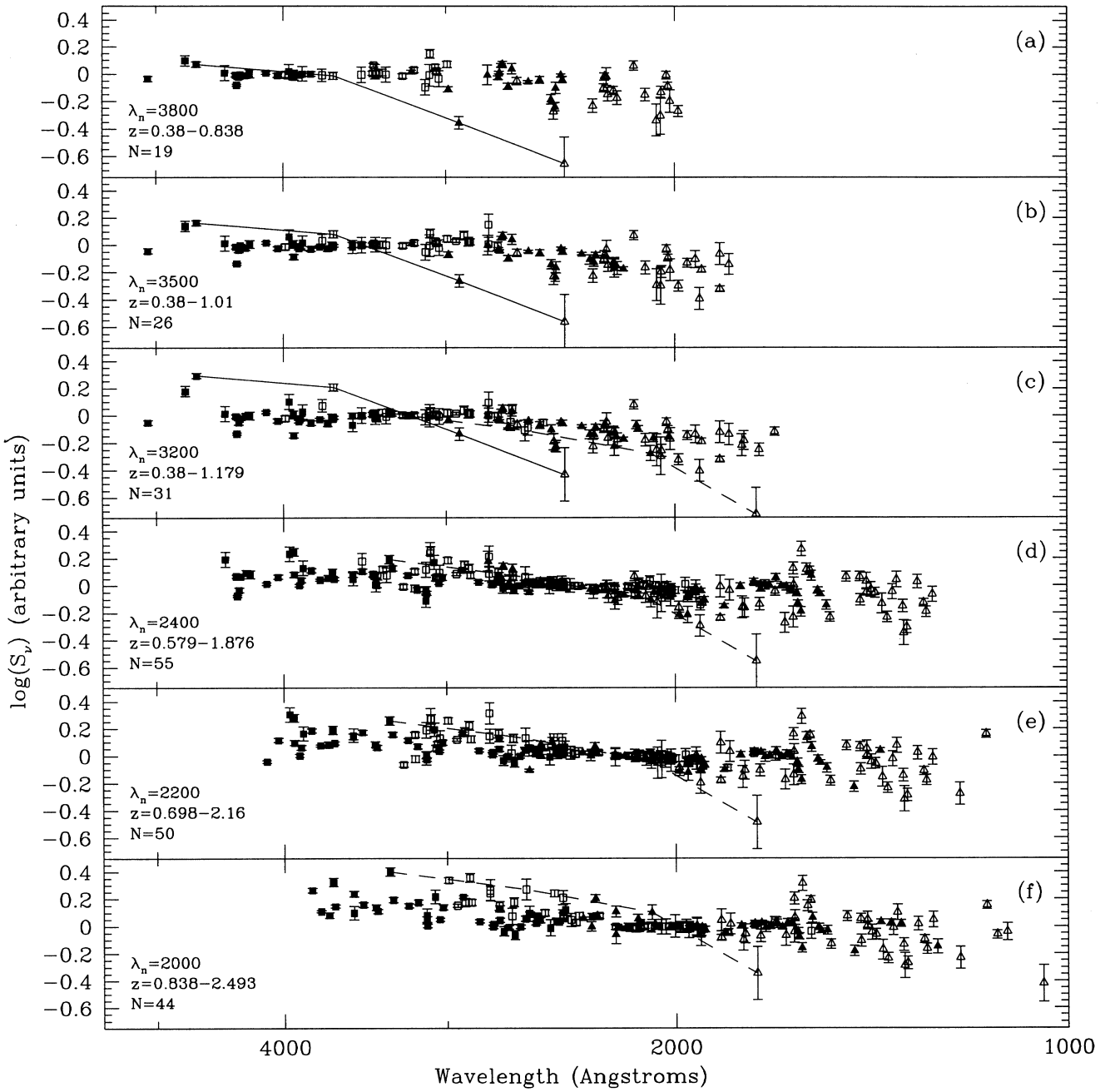

Figure 6. Composite SED for different normalization wavelengths. Spectral points from different optical bands are shown with different symbols. Filled squares, empty squares, filled triangles and empty triangles correspond respectively to *R*-,*V*-,*B*- and *U*-band data. The spectral points of the red quasars B3 0918+381 and B3 1339+472 appear connected on the figure to distinguish their individual SEDs.

cent contribution corresponds to a vertical shift in $\log S_\nu$ (Fig. 6) of 0.04, which is clearly lower than the dispersion of the spectral points in the composites.

Some of the spectral points clearly deviating in the composite SEDs correspond to the two reddest quasars, B3 0918+381 and 1339+472 ($\alpha \leq -1.6$). The extreme red colours of these two sources are uncommon in the sample, as can be seen from Fig. 3, where the symbols for the two sources appear underlined. Both sources show curved spectra in the $\log S_\nu$–$\log \lambda$ plane. B3 0918+381 has an acceptable fit for the power-law model, but this is because of the large-magnitude error at the *U* band. In Fig. 6 the normalized SEDs of these sources are indicated over the remaining spectral points, showing the notorious discrepancy relative to the average composite SEDs. These two sources with peculiar SEDs will not be considered for the discussion in this and the next section.

The overall shape of the composite spectra is found to be very uniform for the different normalizations. The dispersion of the spectral points is artificially reduced near the wavelength λ_n. The spectral points appear to trace predominantly the continuum; only the C IV λ1549 line appears prominent on the composites, as an 'emission feature'. No other emission bumps/lines are apparent from the composites, in agreement with the low contributions expected (Section 4.1). The C IV feature is revealed in the three composites covering its wavelength and arises from the *U*-band

data of various quasars, most of which were mentioned in Section 5 to have likely contamination by this line. The emission feature appears in the broad-band composite displaced to the red, peaking at around 1610 Å. The displacement is around five times lower than the rest-frame width over which the line is detected.

A general trend in Fig. 6, apparent especially from panels (b) to (d), is a steepening of the spectrum from large to short wavelengths, occurring at around 3000 Å. Above this wavelength the SED appears to be rather flat. This trend is less evident in panel (a), probably because of the small number of spectral points at $\lambda < 3000$ Å. The trend is weak in panel (e) and practically disappears in panel (f), but here the number of points with $\lambda > 3000$ Å is small. Panels (d) and (e) appear to show that the SED flattens again below 2000 Å. This trend practically disappears in panel (f), in spite of the large number of points; thus this flattening is not so clear in principle as the steepening at 3000 Å.

6.2 Power-law fits

We have obtained power-law fits of the composite SEDs in the regions above and below the 3000-Å break. The selected ranges were 4500–3000 Å (referred to as 'blue') and 2600–1700 Å (referred to as 'UV'), which roughly correspond to the regions limited by Hβ and Mg II λ2798 and Mg II λ2798 and C IV λ1549. These spectral points were taken as representing the continuum, since the contamination by emission lines/bumps in this range is expected to be very weak. The results of the fits, obtained by least-squares minimization, are listed in Table 5, including for each composite the slopes and their errors, the number of spectral points used and the redshift range of the quasars. Slopes with an asterisk correspond to lower-quality fits, since the spectral points do not cover the whole wavelength range. Fig. 7 shows the spectral index values as a function of λ_n, illustrating its variation between the different composites. The four composite SEDs for which power laws were fitted in both ranges show a steepening from low to high frequency. The differences $\alpha_{blue} - \alpha_{UV}$ for these composites and their errors are listed in Table 5. For the following discussion only the good-quality fits will be considered.

Concerning the 4500−3000 Å range, the spectral indices for all the normalizations are consistent within their errors. The first three normalizations, with $\lambda_n = 3800$, 3500 and 3200 Å, show a better agreement with each other. Averaging the spectral indices for the fits for $\lambda_n = 3800$, 3200 and 2400 Å (the fit for 3500 Å has a large overlap with those for 3200 and 3800 Å) we obtain $\langle\alpha_{blue}\rangle = 0.11 \pm 0.16$.

The high-frequency fits have again best-fitting slopes consistent with each other within the errors. For the high-frequency normalizations at $\lambda_n = 2400$, 2200 and 2000 Å, the spectral indices are very similar, although the ranges of spectral points used do not show a wide overlap. The spectral index for the low-frequency normalization at $\lambda_n = 3200$ Å is steeper. Averaging the slopes obtained for $\lambda_n = 3200$, 2400, 2200 and 2000 Å we find $\langle\alpha_{UV}\rangle = -0.66 \pm 0.15$.

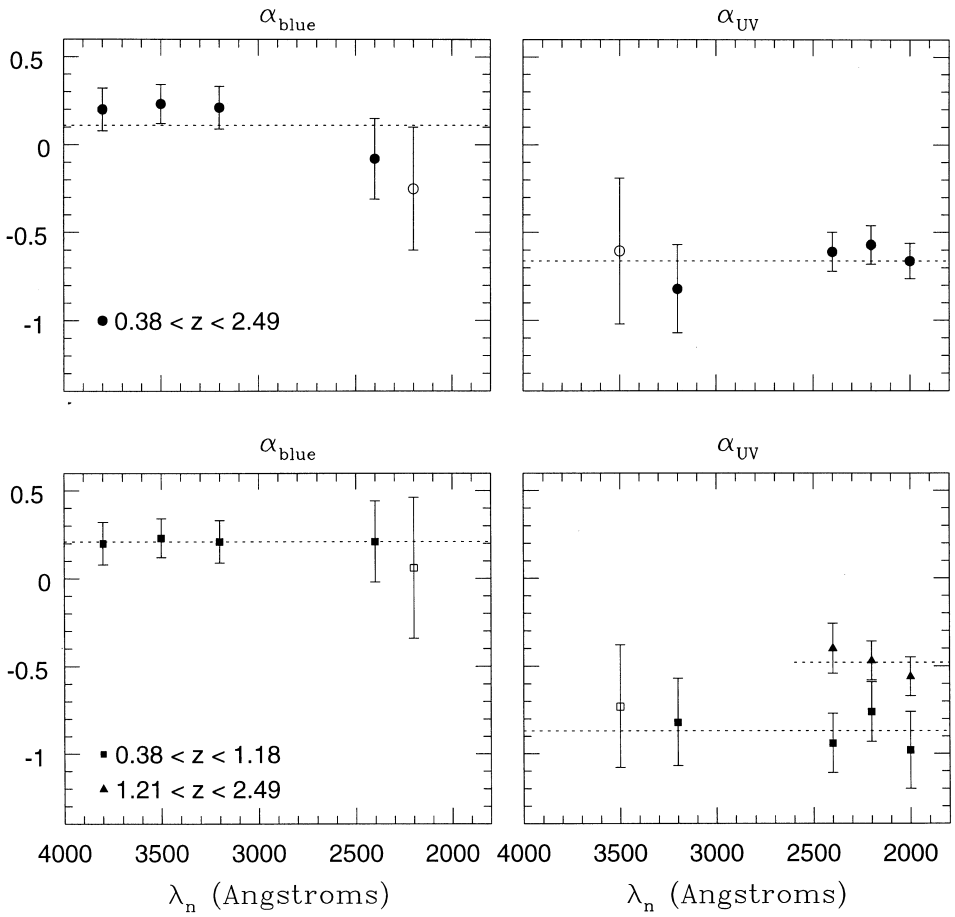

Figure 7. Spectral indices as a function of λ_n. Empty symbols correspond to poor fits. Top panels correspond to the results in Table 5, for quasars of all redshifts, and the bottom panels to the results in Table 6, separating low- and high-redshift quasars.

Table 5. Power-law fits in the intervals 4500–3000 and 2600–1700 Å for quasars in the redshift range 0.38–2.49.

λ_n	α_{blue}	σ	N	z range	α_{UV}	σ	N	z range	$\alpha_{blue}-\alpha_{UV}$	σ
3800	0.20	0.12	34	0.38-0.84						
3500	0.23	0.11	41	0.38-1.01	-0.73*	0.35	38	0.47-1.01	0.96*	0.37
3200	0.21	0.12	45	0.38-1.18	-0.82	0.25	47	0.47-1.18	1.03	0.28
2400	-0.08	0.23	50	0.57-1.32	-0.61	0.11	96	0.57-1.88	0.53	0.25
2200	-0.25*	0.35	36	0.69-1.32	-0.57	0.10	93	0.69-2.16	0.32*	0.36
2000					-0.66	0.10	80	0.83-2.49		

*Lower-quality fits (see text).

Considering the average measured values of α_{blue} and α_{UV} and their errors we find a steepening towards high frequencies $\langle\alpha_{blue}\rangle - \langle\alpha_{UV}\rangle = 0.77 \pm 0.22$.

Although the expected contribution of emission lines/bumps in the ranges used for the power-law fits is low, it is interesting to analyse the possibility that the slope change is artificially produced by contamination by the Fe II bumps at 3100–3400 and 2250–2650 Å, since these features would enhance the emission used for the power-law fits (4500–3000 and 2600–1700 Å) in the regions next to the break, producing a slope change in the observed sense. However, a power-law fit for the whole range from 1700 to 4500 Å for the composites (b) to (d), where the break is more obviously detected, yields a clear excess emission only in the region 2650–3200 Å, i.e. between the two bumps. In fact some excess there could result from Mg II, but if the Fe II bumps were responsible for the slope change, the excess emission should extend over the Fe II ranges 2250–2650 and 3100–3400 Å. Therefore, although some of the broad-band spectral points are expected to include contamination by emission lines and/or bumps, the break in the overall SED detected at ~3000 Å is most likely related to an intrinsic change in the continuum of the quasars. A steepening of the quasar's continuum at 3000 Å was reported by Natali et al. (1998) from spectra of optically selected quasars, and is also found in the composite spectrum of optically selected quasars by Francis et al. (1991). The slopes obtained by Natali et al. (1998) were $\langle\alpha_{blue}\rangle \simeq 0.15$ for the range 2950–5500 Å, and $\langle\alpha_{UV}\rangle \simeq -0.65$ for the range 1400–3200 Å, in good agreement with our values.

6.3 Redshift dependence of the blue/UV continuum shape

A striking characteristic of the best-fitting slopes in Table 5 and Fig. 7 (top panels) is how they keep roughly constant for the normalizations at either side of the break around 3000 Å, suffering the largest variation when the normalization moves from one side of the break to the other. In particular, the change in α_{UV} from $\lambda_n = 3200$ Å to lower values of λ_n is consistent with the description outlined in Section 6.1 of a possible flattening at around 2000 Å for the composites with $\lambda_n = 2400$ and 2200 Å. It is important to note that the change in normalizations from $\lambda_n \geq 3200$ Å to $\lambda_n \leq 2400$ Å in our study implies a substantial *change in the redshifts* of the quasars whose spectral points enter the fits. For instance, whereas the high-frequency fit for $\lambda_n = 3200$ Å comprises 47 spectral points with $0.47 < z < 1.18$, the next composite, with $\lambda_n = 2400$ Å, includes all but one of these points plus 50 additional spectral points from $1.21 < z < 1.88$. For the final composite, with $\lambda_n = 2000$ Å, only 23 out of the 80 spectral points used for the fit are in common with the fit for $\lambda_n = 3200$ Å. A similar variation of the spectral points/redshifts with λ_n occurs for the low-frequency fits, although in this case the low-redshift limit for $\lambda_n = 3800$, 3500 and 3200 Å is similar and the variations of spectral points/redshifts are lower for all the normalizations (see Table 5). It is therefore interesting to analyse whether a dependence of the shape of the continuum spectrum with redshift is present.

From the results of the fits (Table 5, Fig. 7, and see also Fig. 6) we decided to separate the quasar sample into a low-redshift bin with $z < 1.2$ and a high-redshift bin with $z > 1.2$, and perform the power-law fitting for the two subsamples. With the selected limit, all the spectral points used for the normalizations with $\lambda_n > 3000$ Å correspond to the low-redshift bin. The composites with $\lambda_n \leq 2400$ Å include spectral points from quasars in the two redshift bins. Figs 8 and 9 show the composite SEDs for the two quasar subsamples. The results of the power-law fits are given in Table 6 and the variation of the slopes as a function of λ_n is shown in Fig. 7.

Concerning the low-redshift quasars, we find now a better agreement between the slopes of the low-frequency fits obtained for the normalizations on either side of the break. Averaging the values for the normalizations with $\lambda_n = 3800$, 3200 and 2400 Å we find $\langle\alpha_{blue}\rangle = 0.21 \pm 0.16$. For the high-frequency fits there is also a better agreement in α_{UV} between the normalizations at either side of the break. The agreement is caused by the steepening of α_{UV} for the normalizations with $\lambda_n \leq 2400$ Å when high-redshift quasars have been excluded. The average value of α_{UV} is now $\langle\alpha_{UV}\rangle = -0.87 \pm 0.20$. We find now a larger change from α_{blue} to α_{UV}, with $\langle\alpha_{blue}\rangle - \langle\alpha_{UV}\rangle = 1.08 \pm 0.26$. The larger steepening is evident from the comparison of the top and bottom panels of Fig. 7. The good agreement in the slopes obtained for the different normalizations indicates that the selection of λ_n does not affect the derived slopes.

For the high-redshift quasars only the high-frequency region can be studied (see Fig. 9). The average spectral index from the three normalizations is $\langle\alpha_{UV}\rangle = -0.48 \pm 0.12$. Comparing the values of α_{UV} for low- and high-redshift quasars we find a difference $\Delta\langle\alpha_{UV}\rangle = 0.39 \pm 0.23$. This difference, although weak, is larger than the error, and is clearly evident from the results in Table 6 and Fig. 7, and the comparison of Figs 8 and 9. The flattening below around 2000 Å noted in Section 6.1 for the high-frequency normalizations is related to this hardening of α_{UV} for high-redshift quasars.

Our result of a dependence of the spectral index with redshift (in the sense that quasars at $z > 1.2$ tend to be flatter, i.e. harder, than low-redshift ones, in the range 2600–1700 Å) is similar to that found by O'Brien et al. (1988) for an *IUE*-selected sample, with slopes in the region 1900–1215 Å ranging from –0.87 for $z < 1.1$ to –0.46 for $z > 1.1$. We note the remarkable agreement between these values and those obtained for our sample. This trend with redshift was not confirmed by Natali et al. (1998) for their sample of optically selected quasars, although their limits for the detection of a variation were around 0.4, which is comparable to the measured change in the slope found in O'Brien et al. and in this work.

A possible concern with our results is whether the 20 per cent incompleteness of the sample could produce a bias against the inclusion of red quasars at high redshifts. However, the distribution of *R* magnitudes in the range $z = 0.5$–2.5 is roughly constant, and

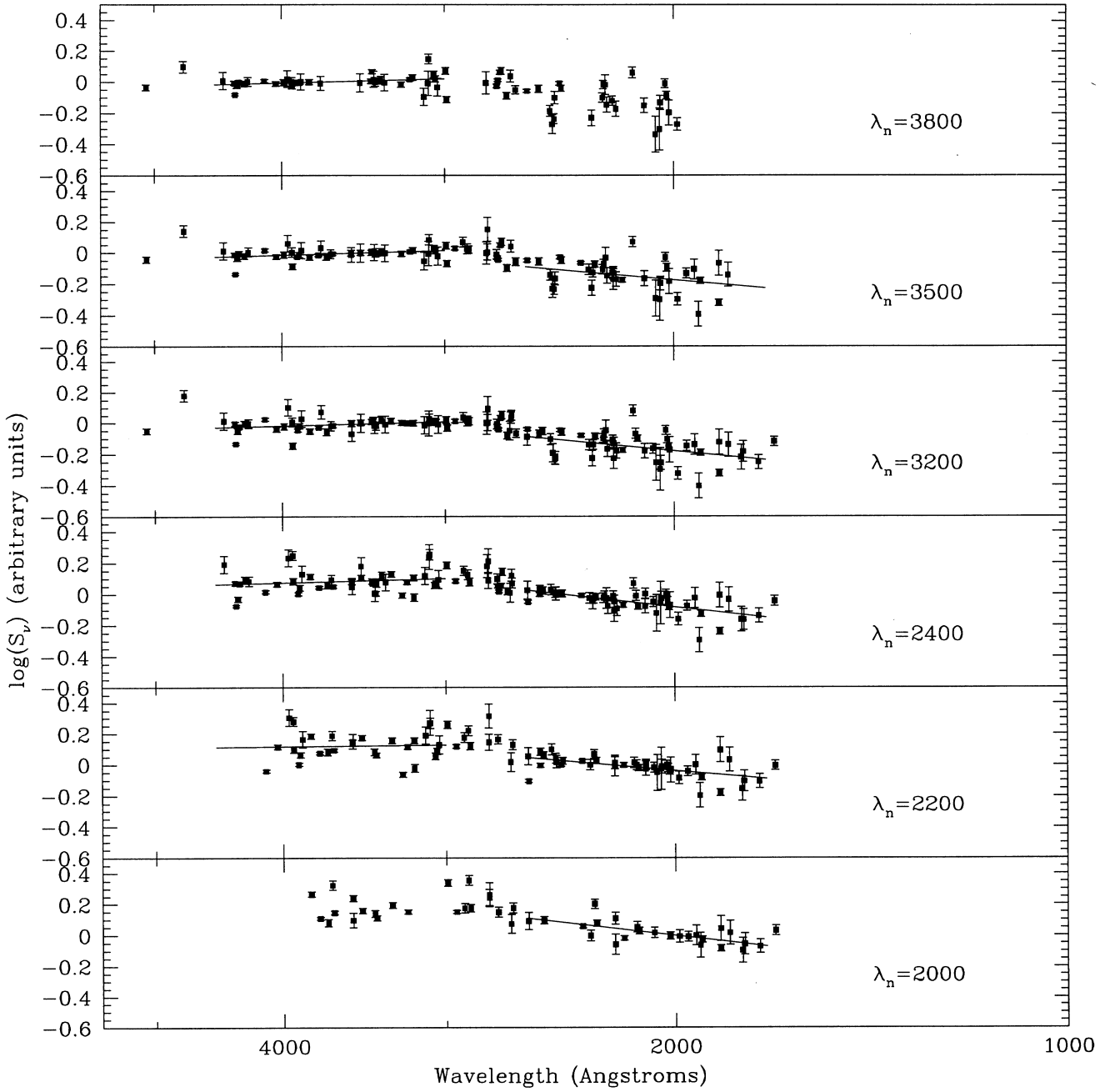

Figure 8. Same as Fig. 6 for quasars with $z < 1.2$. The straight lines show the best-fitting power laws in the regions 4500–3000 Å and 2600–1700 Å.

Table 6. Power-law fits for quasars in the redshift range 0.38–1.18 (upper part) and 1.21–2.49 (bottom part).

λ_n	α_{blue}	σ	N	z range	α_{UV}	σ	N	z range	$\alpha_{blue} - \alpha_{UV}$	σ
3800	0.20	0.12	34	0.38-0.84						
3500	0.23	0.11	41	0.38-1.01	-0.73*	0.35	38	0.47-1.01	0.96*	0.37
3200	0.21	0.12	45	0.38-1.18	-0.82	0.25	47	0.47-1.18	1.03	0.28
2400	0.21	0.23	43	0.57-1.18	-0.94	0.17	48	0.57-1.18	1.15	0.29
2200	0.06*	0.40	29	0.69-1.18	-0.76	0.17	41	0.69-1.18	0.82*	0.43
2000					-0.98	0.22	24	0.83-1.18		
2400					-0.40	0.14	48	1.21-1.88		
2200					-0.47	0.11	52	1.21-2.16		
2000					-0.56	0.11	56	1.21-2.49		

*Lower-quality fits (see text).

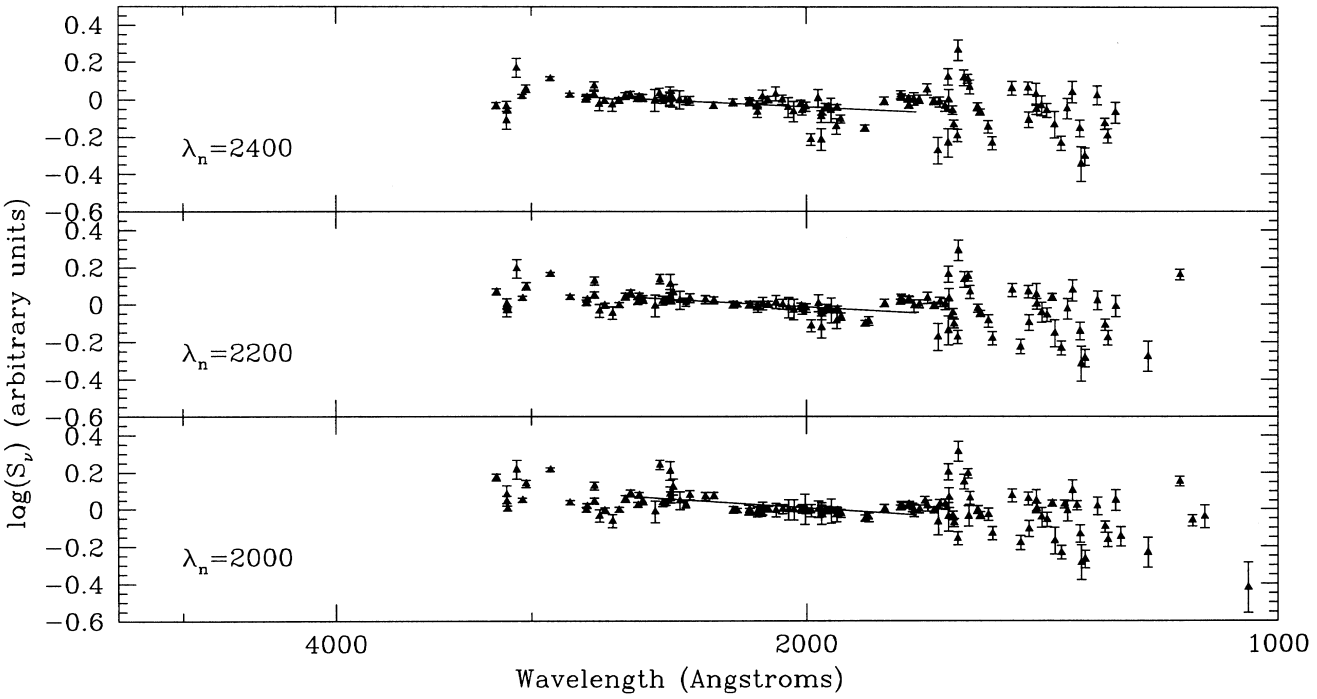

Figure 9. Same as Fig. 6 using only spectral points from quasars with $z > 1.2$.

does not suggest that the fraction of missed quasars ($R > 20$) should be higher at the higher redshifts. On the other hand, five good B3-VLA quasar candidates excluded from the B3-VLA Quasar Sample were present on the blue POSS-I plate but not on the red POSS plate. Since the magnitude limit for POSS blue is around 20.5–21, these quasars have $B - R$ colours similar or bluer than the average value for the quasars in the sample ($B - R = 0.64$, Section 4.2). Although this number of quasars is small, it illustrates the presence of blue or normal colours among the missed quasars. Since the incompleteness does not appear to be biased towards the exclusion of red quasars at high redshifts, the α_{UV}–z trend is likely to be a real effect, not originated by incompleteness.

6.4 Relation of the blue/UV continuum shape to radio power

Fig. 10 presents the P_{408}–z diagram for the 73 quasars observed for this work. In agreement with the expectations for flux-limited samples, high-redshift quasars tend to have higher radio powers than low-redshift ones, although the B3-VLA Quasar Sample is not strictly a flux-limited one (see Section 2). Using Spearman's correlation coefficient r_S, we find for the trend $r_S = 0.52$, with a significance level $P > 99.999$. In order to check whether the α_{UV}–z trend could arise from an intrinsic α_{UV}–P_{408} correlation and the P_{408}–z trend, we performed an analysis similar to the one presented in Sections 6.2 and 6.3, obtaining separated power-law fits for a 'high-radio-power subsample' and a 'low-radio-power subsample'. Instead of considering several composites, the dependence on radio power was analysed using only the composite with $\lambda_n = 2400$ Å. This composite includes the largest number of quasars, and the redshift distribution comprises low- as well as high-redshift ones, with a median z of 1.15, similar to that of the whole sample.

The composite with $\lambda_n = 2400$ Å includes 54 quasars (excluding B3 0918+381). The median of P_{408} is $10^{34.85}$ erg s^{-1} Hz^{-1} and this value was used as the division limit between low and high radio power. The low-power quasars have a mean redshift of 1.00 and a mean radio power $10^{34.48}$ erg s^{-1} Hz^{-1}, and the same parameters for the high-power quasars are 1.35 and $10^{35.19}$ erg s^{-1} Hz^{-1}. The results of the derived spectral indices α_{UV} for the two subsamples are listed in Table 7. The table includes for comparison the α_{UV} values obtained for all the quasars and for the subsamples separated by redshift, for the same composite. The third column of the table gives $\Delta\alpha_{UV}$ and its error for each pair of subsamples with a varying parameter (z or P_{408}), and the last column gives the probability that the difference in slope is statistically significant.

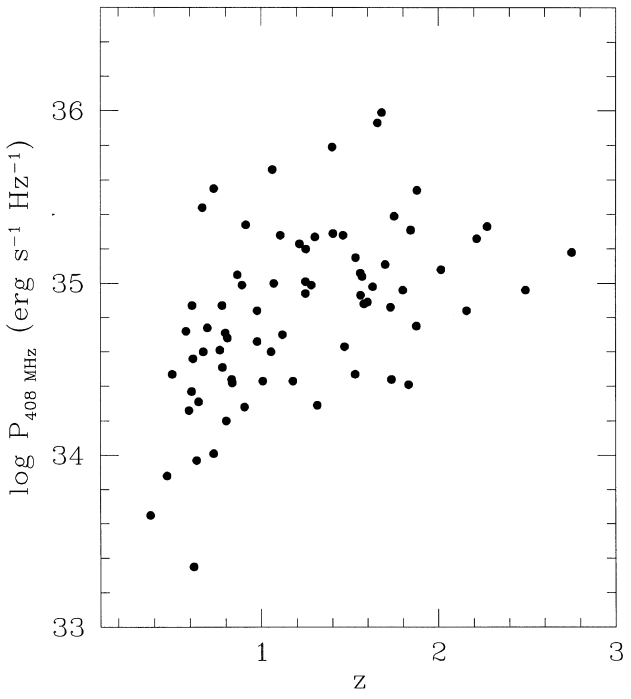

Figure 10. $P_{408\,MHz}$ versus redshift for the 73 B3-VLA quasars observed for this work.

Table 7. α_{UV} for the composite with $\lambda_n = 2400$ Å and different subsamples, separated by redshift, radio power and blue/UV luminosity.

	α_{UV}	$\Delta(\alpha_{UV})$	Significance of the slope change
All z	-0.61 ± 0.11		
$z < 1.2$	-0.94 ± 0.17	0.54 ± 0.22	98.84 per cent
$z > 1.2$	-0.40 ± 0.14		
$P_{408} < 10^{34.85}$	-0.71 ± 0.18	0.20 ± 0.23	27 per cent
$P_{408} > 10^{34.85}$	-0.51 ± 0.14		
$L_{2400} < 10^{30.67}$	-0.76 ± 0.18	0.30 ± 0.22	89 per cent
$L_{2400} > 10^{30.67}$	-0.46 ± 0.13		

The largest difference in α_{UV} and the highest significance is found for the subsamples separated by z, with $\Delta\alpha_{UV} = 0.54 \pm 0.22$, and 98.84 per cent significance (F-test). For the subsamples separated by P_{408} the difference in α_{UV} is lower than the errors. The trend α_{UV}–z is therefore unlikely to be a secondary correlation from an intrinsic α_{UV}–P_{408} correlation in conjunction with the P_{408}–z trend. Moreover, the last trend is less significant for the group of 54 quasars in the $\lambda_n = 2400$ Å composite ($r_S = 0.44$ and $P = 99.906$). This weak trend explains in fact the reverse result, i.e. that the α_{UV}–z trend in combination with the P_{408}–z trend does not cause a α_{UV}–P_{408} trend.

6.5 Relation of the blue/UV continuum shape to blue/UV luminosity

The possible relation between α_{UV} and the blue/UV luminosity was also investigated. In order to construct each composite SED we had to interpolate the flux density at the normalization wavelength λ_n, and therefore we could obtain the monochromatic luminosity at λ_n straightforwardly. The possible trend $L_{blue/UV}$–α_{UV} was analysed in the same way as for the P_{408}–α_{UV} trend, measuring α_{UV} in the composite with $\lambda_n = 2400$ Å for two subsamples separated by L_{2400}. The separation value was set at $L_{2400} = 10^{30.67}$ erg s^{-1} Hz^{-1}, which is the median value for the quasars in the composite. The values of α_{UV} (Table 7) indicate a weak flattening with luminosity, only slighly larger than the errors, but significant from the F-test, with $P = 89$ per cent. The significance is lower than that found for the α_{UV}–z trend.

Fig. 11 shows L_{2400} versus z for the quasars in the same composite. A clear correlation is found, in the sense that high-redshift quasars are more luminous, similar to the trend with radio power. A Spearman correlation gives $r_S = 0.52$ and significance 99.994 per cent. Therefore the three parameters α_{UV}, z and L_{2400} are correlated with each other, and in principle it is impossible to determine which are primary and which are secondary correlations. The quasars with luminosities below the limit of $10^{30.67}$ erg s^{-1} Hz^{-1} have a mean redshift and luminosity of 1.01 and $10^{30.27}$ erg s^{-1} Hz^{-1}, and the same parameters for the luminous quasars are 1.33 and $10^{31.02}$ erg s^{-1} Hz^{-1}.

Wandel & Petrosian (1988) obtained predictions of the expected UV slope versus UV luminosity for various accretion disc models, spanning a range of values for the black hole mass, accretion rate and viscosity parameter. They found that the effect of a flattening of the spectrum for the more luminous quasars (or at higher redshifts), reported by O'Brien et al. (1988), could be explained as evolution along curves of constant black hole mass, with accretion rate decreasing with time. The emitted spectrum for these models under the assumption of constant black hole mass is less luminous and more steep in the UV as the accretion rate decreases, and a decrease in accretion rate with time could explain the observed L_{UV}–z and α_{UV}–z trends. Our data show the same trend of a flattening of α_{UV} with z and L_{UV}, as well as a L_{UV}–z correlation, and therefore the same interpretation could apply. The diagrams $\alpha_{UV} - L_{UV}$ presented by Wandel & Petrosian (1988) correspond to a slope in the range 1500–1000 Å and the luminosity at 1450 Å. We have represented in these diagrams the average slope for low-redshift and high-redshift quasars (separation at $z = 1.2$), using the composite with $\lambda_n = 2400$ Å, and the 2600–1700 Å slopes listed in Table 7. The luminosities were obtained by transforming the average values at 2400 Å to 1450 Å, adopting the measured slopes. Although we use a slope different from that of the models, at least for high-redshift quasars the slope does not appear to change between the two ranges (Fig. 9). A straight line connecting the location of the two subsamples on the α_{UV}–L_{UV} plane would run approximately parallel to the curves of constant black hole mass, with $\dot{m}$ increasing in the same direction as the redshift. Therefore our results appear to be consistent with the interpretation outlined above, and the comparison with the models yields a roughly constant black hole mass, in the range $M \simeq 10^{8.2-8.5}\,M_\odot$, and accretion rates (in units of the Eddington value) ranging from $\dot{m} \simeq 1$ for the quasars with $z = 0.6$–1.2 to $\dot{m} \simeq 10$ for the quasars with $z = 1.2$–1.9.

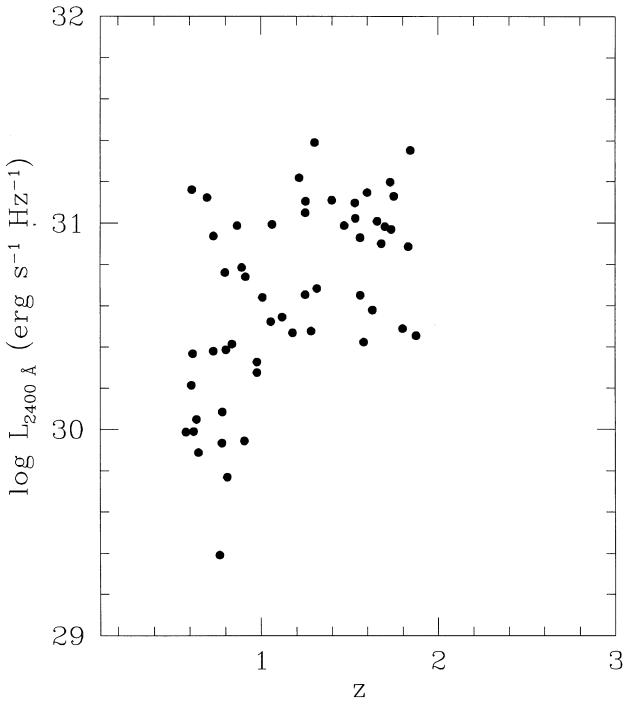

Figure 11. $L_{2400\,Å}$ versus z for the 54 quasars with measured (interpolated) flux density at 2400 Å.

7 THE CORRELATION BETWEEN BLUE/UV LUMINOSITY AND RADIO POWER

Fig. 12(a) shows L_{2400} versus P_{408} for the 54 quasars of the $\lambda_n = 2400$ Å composite. L_{2400} and P_{408} are strongly correlated, with $r_S = 0.62$ and $P > 99.9999$ per cent. The optical completeness of the sample is high and we do not expect important selection effects in the optical that could explain the correlation. The correlation could be in principle artificially induced by independent evolution of both parameters with redshift. In fact the quasars with

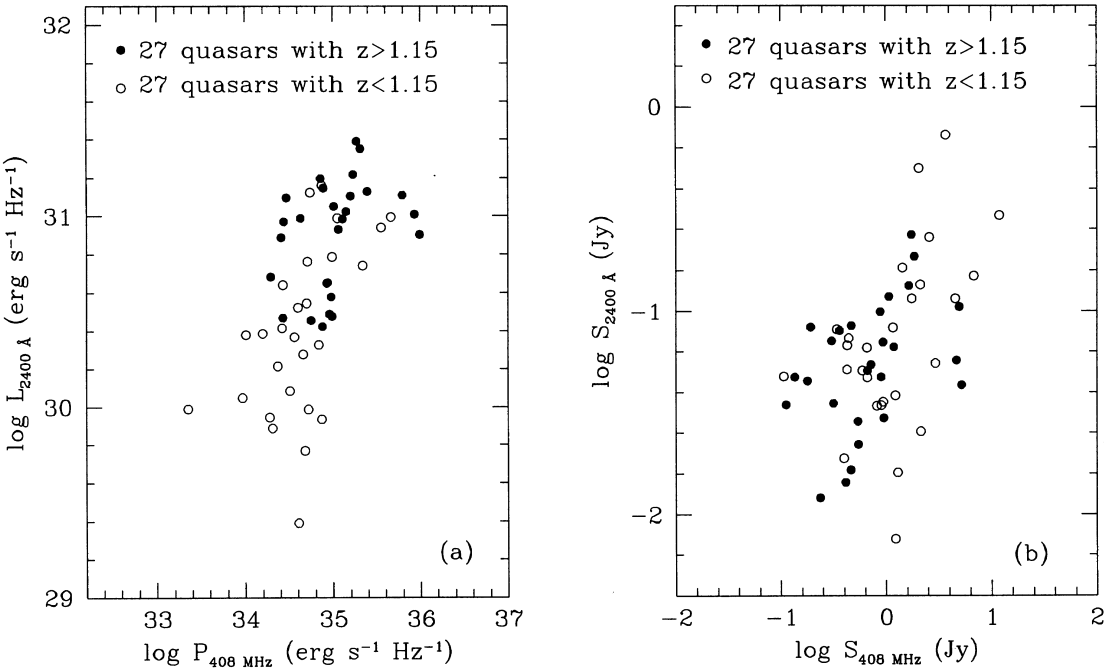

Figure 12. Panel (a): L_{2400} versus P_{408} for 54 B3-VLA quasars in this work. Panel (b): S_{2400} versus S_{408} flux densities for the same quasars. For the radio fluxes we used the k-correction $C = -(1+\alpha)\log(1+z)$, where α is the radio spectral index between 408 and 1460 MHz given by Vigotti et al. (1989). For the flux densities at 2400 Å the k-correction adopted was $C = -\log(1+z)$.

high blue/UV luminosity tend to have large redshifts and those weaker tend to have low redshifts, and a similar behaviour occurs for the radio power. However, this alternative is ruled out by the redshift distribution in Figure 12(a), showing that the half sub-sample with lower redshifts shows a similar L_{2400}–P_{408} trend as the whole sample (with unrestricted z). The correlation is confirmed in the flux-flux plane in Fig. 12(b), with $r_S = 0.47$ and $P = 99.966$ over two decades in both radio and blue/UV flux.

The most likely origin for the radio–optical correlation is therefore a direct link between the blue/UV emission of the quasar nucleus, related to the accretion process, and the radio synchrotron emission at 408 MHz. A similar correlation was reported by Serjeant et al. (1998) on the basis of complete samples of radio-steep-spectrum quasars (from Molonglo, 3CR and the Bright Quasar Survey), in the redshift range 0.3–3. A linear fit for our data in the $\log L_{2400}$–$\log P_{408\,MHz}$ plane yields $L_{2400} \propto P_{408\,MHz}^{0.52\pm0.10}$, with a dispersion in blue/UV magnitudes of ~0.9, for quasars in the redshift range 0.6–1.9. The best-fitting slope is very similar to that obtained by Serjeant et al. (1998), with $L_B \propto P_{408\,MHz}^{0.6\pm0.1}$, although these authors give a larger dispersion, ~1.6 mag.

In the light of an intrinsic correlation between radio power and blue/UV luminosity we can investigate in more detail the relations between α_{UV}, z, P_{408} and L_{2400} reported in Sections 6.4 and 6.5. The lack of an α_{UV}–P_{408} trend is still acceptable, in spite of an α_{UV}–L_{2400} correlation, since the latter is weak. The trends P_{408}–z and L_{2400}–z are likely related through the radio–optical correlation.

If the correlation L_{2400}–z was predominantly intrinsic, rather than resulting from selection effects, the three correlations L_{2400}–z, L_{2400}–α_{UV} and α_{UV}–z could be explained with AD models with constant black hole mass and $\dot{m}$ increasing with redshift (see Section 6.5). The correlation L_{2400}–P_{408} would then imply that the P_{408}–z trend is, at least in part, intrinsic. If the trend P_{408}–z was the result of a selection effect, preventing the detection of low-power sources at high z, the trend L_{2400}–z could also be the result of this effect, rather than cosmic evolution. In this case one of the correlations α_{UV}–z or α_{UV}–L_{2400} could be induced by the other, in combination with the L_{2400}–z trend. According to the models by Wandel & Petrosian (1988), a correlation L_{2400}–α_{UV} in the observed sense would arise naturally if, keeping a constant black hole mass, the parameter $\dot{m}$ varies. We cannot exclude however the reverse interpretation, i.e. that the intrinsic trend is for α_{UV}–z and α_{UV} is not directly dependent on blue/UV luminosity or radio power. O'Brien et al. (1988) found from a joint regression analysis for the three parameters that the dominant correlation for their data was between α_{UV} and z.

8 CONCLUSIONS

In this work we present optical photometry of a sample of radio quasars in the redshift range $z = 0.4$–2.8, around 80 per cent complete, aimed at studying their spectral energy distribution in the blue/UV range. The $U-R$, $B-R$ and $U-V$ colours do not vary substantially with redshift, and the average values are $\langle U-R\rangle = -0.08$ with rms 0.45, $\langle B-R\rangle = 0.64$ with rms 0.27 and $\langle U-V\rangle = -0.38$ with rms 0.42. Two quasars at $z = 0.50$ and 1.12 stand out for being particularly red, with $U-R > 1$.

Power-law fits to the SEDs of the quasars with available photometry in the four bands yield spectral indices ranging from ~0.4 to ~− 1.7. The distribution of slopes is asymmetric, with a tail to steep spectral indices. Excluding the sources in the tail, the distribution is well modelled as a Gaussian with mean and dispersion of –0.21 and 0.34 respectively.

Composite SEDs normalized at various wavelengths were constructed from the sample (excluding the two red quasars), and the overall shape of the composites was found to be very similar for the different normalizations. The only emission feature revealed from the composites was the C IV λ1549 line. This result is in agreement with the expectations from the EW measurements of broad

emission lines and Fe II bumps of steep-spectrum radio quasars, which predict, for the bandwidths and redshifts in our work, the largest contribution for the C IV line. For other emission features, like Mg II, C III] and the Fe II bumps at 2250–2650 and 3100–3800 Å, the expected average contributions to the broad-band fluxes are below 10 per cent. The composite SEDs show a clear steepening towards high frequencies at around 3000 Å, which cannot be explained by line contamination and most likely reflect a trend of the continuum. Parametrizing the SEDs as power laws we obtained an average $\langle\alpha_{\rm blue}\rangle = 0.11 \pm 0.16$ for the range 4500–3000 Å and $\langle\alpha_{\rm UV}\rangle = -0.66 \pm 0.15$ for 2600–1700 Å.

Separating the quasar sample into two redshift bins, with the cut at $z = 1.2$, a better agreement was found between the values of $\alpha_{\rm blue}$ and $\alpha_{\rm UV}$ obtained for the different normalizations, and a hardening of $\alpha_{\rm UV}$ with redshift emerged, with $\langle\alpha_{\rm UV}\rangle = -0.87 \pm 0.20$ for $z < 1.2$ and $\langle\alpha_{\rm UV}\rangle = -0.48 \pm 0.12$ for $z > 1.2$. The average spectral index $\alpha_{\rm blue}$ for the low-redshift quasars is $\langle\alpha_{\rm blue}\rangle = 0.21 \pm 0.16$, and therefore these quasars show a steepening from the blue to the UV range $\langle\alpha_{\rm blue}\rangle - \langle\alpha_{\rm UV}\rangle = 1.08 \pm 0.26$. The composite SEDs for the high-redshift quasars do not cover the region above 3000 Å, and therefore the presence of a similar break for these quasars could not be analysed from the present data.

Correlations were also found between luminosity at 2400 Å and redshift, and between radio power and redshift. Separating the quasar sample into two bins of low and high luminosity at 2400 Å, a trend was found between $\alpha_{\rm UV}$ and L_{2400} (89 per cent significant). The quasar sample shows also an intrinsic correlation between L_{2400} and P_{408} ($r_{\rm S} = 0.62$ and $P > 99.9999$), similar to that recently reported by Serjeant et al. (1998) for a sample of steep-spectrum quasars.

The observed trends L_{2400}–$\alpha_{\rm UV}$, L_{2400}–z and $\alpha_{\rm UV}$–z appear to be consistent with the predictions from AD models for the case of constant black hole mass and accretion rate increasing with z (Wandel & Petrosian 1988), with $M_{\rm BH} \simeq 10^{8.2-8.5}\,{\rm M}_{\odot}$, and accretion rates (in units of the Eddington value) ranging from $\dot{m} \simeq 1$ for $z = 0.6$–1.2 to $\dot{m} \simeq 10$ for $z = 1.2$–1.9. An alternative interpretation is that the P_{408}–z and L_{2400}–z trends arise predominantly from a selection effect, due to the radio flux limits of the sample. In this case one of the correlations, $\alpha_{\rm UV}$–z or $\alpha_{\rm UV}$–L_{2400}, could be induced by the other, in combination with the L_{2400}–z trend. The observed $\alpha_{\rm UV}$–L_{2400} correlation is consistent with the predictions from the AD models by Wandel & Petrosian assuming a constant black hole mass and a range of accretion rates, although in this case the accretion rate does not need to be correlated with z. We cannot exclude however that the intrinsic correlation is $\alpha_{\rm UV}$–z, with $\alpha_{\rm UV}$ not being physically related to the blue/UV luminosity.

ACKNOWLEDGMENTS

The 1.0-m JKT telescope is operated on the island of La Palma by the Isaac Newton Group in the Spanish Observatorio del Roque de los Muchachos of the Instituto de Astrofísica de Canarias. The 2.2-m telescope, at the Centro-Astronómico Hispano-Alemán, Calar Alto, is operated by the Max-Planck-Institute for Astronomy, Heidelberg, jointly with the Spanish Comisión Nacional de Astronomía. RC, JIGS and SFS acknowledge financial support by the DGES under project PB95-0122 and by the Comisión Mixta Caja Cantabria–Universidad de Cantabria. SFS wants to thank the FPU/FPI programme of the Spanish MEC for a fellowship.

REFERENCES

Baker J. C., Hunstead R. W., 1995, ApJ, 452, L95. Erratum: ApJ, 468, L131
Boroson T. A., Green R. F., 1992, ApJS, 80, 109
Browne I. W. A., Wright A. E., 1985, MNRAS, 213, 97
Burnstein D., Heiles C., 1982, AJ, 87, 1165
Carballo R., Sánchez S. F., González-Serrano J. I., Vigotti M., Benn C., 1998, AJ, 115, 1234
Cristiani S., Vio R., 1990, A&A, 227, 385
Czerny B., Elvis M., 1987, ApJ, 321, 305
Elvis M. et al., 1994, ApJS, 95, 1
Ficarra A., Grueff G., Tomassetti G., 1985, A&AS, 59, 255
Francis P. J., Hewett P. C., Foltz C. B., Chaffee F. H., Weymann R. J., Morris S. L., 1991, ApJ, 373, 465
Green P. J., 1998, ApJ, 498, 170
Hewett P. C., Foltz C. B., Chaffee F. H., Francis P. J., Weymann R. J., Morris S. L., Anderson S. F., MacAlpine G. M., 1991, AJ, 101, 1121
Johnson H. L., 1966, ARA&A, 4, 193
Landolt A. U., 1992, AJ, 104, 340
Malkan M. A., 1983, ApJ, 268, 582
Natali F., Giallongo E., Cristiani S., La Franca F., 1998, AJ, 115, 397
O'Brien P. T., Gondhalekar P. M., Wilson R., 1988, MNRAS, 233, 801
Rieke G. H., Lebofsky M. J., 1985, ApJ, 288, 618
Sanders D. B., Phinney E. S., Neugebauer G., Soifer B. T., Mathews K., 1989, ApJ, 347, 29
Serjeant S., Rawlings S., Maddox S. J., Baker J. C., Clements D., Lacy M., Lilje P. B., 1998, MNRAS, 294, 494
Vigotti M., Grueff G., Perley R., Clark B. G., Bridle A. H., 1989, AJ, 98, 419
Vigotti M., Vettolani G. V., Merighi R., Lahulla J. F., Pedani M., 1997, A&AS, 123, 1
Wamsteker W., 1981, A&A, 97, 329
Wandel A., Petrosian V., 1988, ApJ, 329, L11
Willott C. J., Rawlings S., Blundell K. M., Lacy M., 1998, MNRAS, 300, 625
Wills B. J., Netzer H., Wills D., 1985, ApJ, 288, 94
Zheng W., Kriss G. A., Telfer R. C., Grimes J. P., Davidsen A. F., 1997, ApJ, 475, 469

This paper has been typeset from a TEX/LATEX file prepared by the author.